Large tunable valley splitting in edge-free graphene quantum dots on boron nitride

DOI:
10.1038/s41565-018-0080-8

Document Version
Accepted author manuscript

Large tunable valley splitting in edge-free graphene quantum dots on boron nitride

Nils M. Freitag[1], Tobias Reisch[2], Larisa A. Chizhova[2], Peter Nemes-Incze[1,3], Christian Holl[1], Colin R. Woods[4], Roman V. Gorbachev[4], Yang Cao[4], Andre K. Geim[4], Kostya S. Novoselov[4], Joachim Burgdörfer[2], Florian Libisch[2], and Markus Morgenstern[1]

[1]II. Institute of Physics B and JARA-FIT, RWTH Aachen University, Otto-Blumenthal-Straße, 52074 Aachen, Germany
[2]Institute for Theoretical Physics, TU Wien, Wiedner Hauptstraße 8-10, 1040 Vienna, Austria
[3]Centre for Energy Research, Institute of Technical Physics and Materials Science, Lendület - Topology in Nanomaterials Research Group, 1121 Budapest, Konkoly-Thege way 29-33, Hungary
[4]School of Physics & Astronomy, University of Manchester, Manchester, United Kingdom

Coherent manipulation of binary degrees of freedom is at the heart of modern quantum technologies. Graphene, the first atomically thin 2D material, offers two binary degrees: the electron spin and the valley degree of freedom. Efficient spin control has been demonstrated in many solid state systems, while exploitation of the valley has only recently been started without control for single electrons. Here, we show that van-der Waals stacking of 2D materials offers a natural platform for valley control due to the relatively strong and spatially varying atomic interaction between adjacent layers. We use an edge-free graphene quantum dot induced by the tip of a scanning tunneling microscope and demonstrate a valley splitting, which is tunable from -5 meV to $+10$ meV (including valley inversion) by sub-10-nm displacements of the quantum dot position. This boosts controlled tuning of the valley splitting by more than one order of magnitude. The tunable inversion of spin and valley states should enable coherent superposition of these degrees of freedom as a first step towards graphene-based qubits.

A central requirement for the exploitation of the binary degrees of freedom of a single electron is its control by electrical means as favorable for scalability.[1] This has been realized for spin systems using, e.g., small shifts of the electron spin within the field of a nano-magnet [2, 3]. The valley degree of electrons has recently been detected in transport experiments on graphene [4, 5, 6, 7, 8, 9], but its control on the single electron level has not been achieved. Competing systems, such as Si [10], reveal only very small tuning ranges of the valley splitting by less than 0.5 meV [5, 11, 12, 13, 14, 15].

The valley degree of freedom in graphene is a consequence of the honeycomb structure with its two atoms within the unit cell [16, 17]. Hence, breaking the equivalence of the two atoms (sublattice symmetry breaking) is a natural way to break the valley degeneracy as a starting point for tuning [18]. Van-der Waals stacking of 2D materials offers this possibility by a different stacking of the two graphene atoms to the support atoms. This stacking moreover spatially varies due to the different lattice constants of the adjacent materials.[19, 20, 21] This implies a spatially varying valley splitting, which we exploit in our experiment.

Therefore, we use an edge-free graphene quantum dot (QD) induced by the tip of a scanning tunneling microscope (STM) [22]. We have recently demonstrated smoothly confined Dirac fermions in such a QD by combining the electric field of the tip with a perpendicular magnetic field B (Fig. 1a) [22]. The B field quantizes the continuous spectrum of graphene in terms of Landau levels (LLs, LL spacing ≈ 100 meV at $B = 7$ T) [18]. The electric field of the tip exploits the energy gaps between LLs to achieve edge-free confinement, i.e., it shifts energy levels from the LLs into the gap [22]. We thereby overcome the well-known problem of edge localization within etched graphene QDs [23]. By confining without resorting to physical edges, these dots preserve the two-fold valley and spin symmetries of pristine graphene (Fig. 1b, d).

The charging of the confined levels has been directly measured by tuning the voltage of the STM tip such that the states cross the Fermi level E_F. This revealed the most regularly spaced charging sequence of graphene QDs achieved to date [22]. The found level separations have been reproduced with the help of tight binding (TB) calculations, such that the charging peaks could be attributed to LLs and to particular orbital and valley states. We observe quadruplets of charging peaks belonging to a single orbital quantum number of the dot and a partial splitting of single quadruplets into two doublets indicating the lifting of the valley degeneracy (Fig. 1b, d, e). This identification of the multiplet character goes far beyond the results achieved by chemical etching of monolayer graphene QDs [23] or double-sided gating of bilayer graphene QDs [24, 25, 26].

Movable quantum dot

Here, we investigate the nanoscale variation of the charging sequence in detail. We use a heterostructure comprised of a SiO_2/graphite support, a hexagonal boron nitride (hBN) substrate, and an active graphene layer on top which are as-

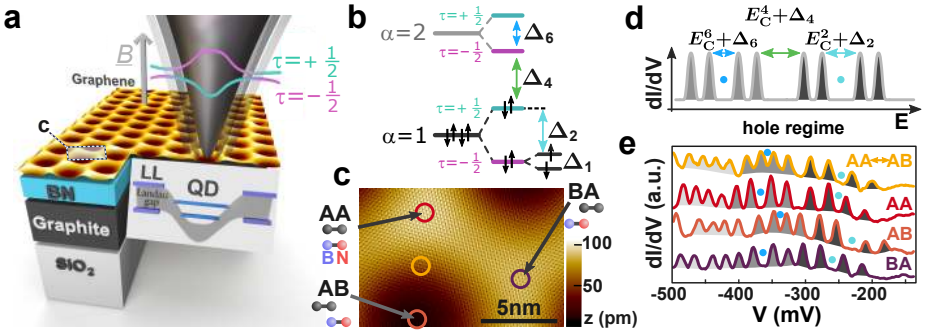

Figure 1: **Edge free quantum dot. (a)** Sketch of the experiment: colored blocks on the left show the stacking sequence SiO_2/Graphite/hBN/Graphene [22]. The STM tip (grey cone) is moved above graphene deposited on BN with its hexagonal lattice collinearly aligned with that of BN (brown-yellow STM image with BN-induced superstructure, $V = 300\,\mathrm{mV}$, $I = 1\,\mathrm{nA}$). A perpendicular $\underline{B}$ field (7 T, grey arrow) leads to Landau levels (LL, purple lines) and corresponding Landau gaps (grey area). The electric field of the tip induces band bending (curvature of Landau gap), leading to confined states (blue lines), hence, to a quantum dot (QD). The QD is moved by moving the STM tip above the superstructure (light grey areas around the cone). This modifies the confined state energies as the valley levels $\tau = 1/2$ and $\tau = -1/2$ associated with the K and K' points of the unperturbed band structure (cyan and magenta lines). The rectangle marked **c** indicates the area shown in magnification in **c**. **(b)** Schematic energy level diagram of the QD. The two orbital levels $\alpha = 1$ and $\alpha = 2$ exhibit valley splitting $E_{\alpha,\tau=+1/2,\sigma} - E_{\alpha,\tau=-1/2,\sigma}$. The Zeeman splitting $E_{\alpha,\tau,\sigma=+1/2} - E_{\alpha,\tau,\sigma=-1/2}$ is small ($\simeq 800\ \mu$eV) and only shown for the lowest valley state. The resulting energy distances Δ_n between adjacent levels are labeled with consecutive n. **(c)** Atomically resolved STM image of rectangular area marked in **a**, $V = 137\,\mathrm{mV}$, $I = 0.3\,\mathrm{nA}$. Different stacking areas (AA, AB, BA) are indicated by arrows with stick and ball models below the labels (C: gray, B: blue, N: red). Colored rings mark the positions of spectra in **e**. **(d)** Sketch of expected dI/dV peak sequence for hole charging according to the level diagram in **b** using the same colored arrows and the same Δ_n; E_C^n: n^{th} charging energy. Blue dots highlight valley gaps. **(e)** dI/dV spectra recorded at the positions encircled by the same color in **c** with corresponding stackings marked (AA↔AB: between AA and AB). Quadruplets of charging peaks, belonging to the same orbital, are shaded equally. Blue dots mark valley transitions. Predominant quadruplet sequences (yellow spectrum), predominant doublet sequences (purple spectrum), or a mixture of both (red and orange spectra) appear, $V_{\mathrm{stab}} = 1\,\mathrm{V}$, $I_{\mathrm{stab}} = 700\,\mathrm{pA}$, $V_{\mathrm{mod}} = 4.2\,\mathrm{mV_{rms}}$, $B = 7$ T, $T = 8$ K.

sembled by the dry stacking method [27, 28] (Fig. 1a). The hexagonal graphene and hBN lattices are collinear in order to create a hexagonal superlattice with

lattice constant $a = 13.8$ nm originating from the lattice mismatch of graphene and hBN.[20] Different stacking regions of the C atoms with respect to the B and N atoms (Fig. 1c) naturally lead to a spatially varying adhesion energy as well as to a spatially varying sublattice symmetry breaking of graphene due to the inequivalent binding sites.[29] The resulting structure has been extensively discussed in the literature [30, 31, 32, 33, 34, 35, 36, 37, 38]. It is known that the most attractive interaction is in the AB areas (Fig. 1c) leading to stretched central regions of graphene with AB stacking and closest contact to the hBN. These areas are surrounded by compressed graphene ridges of different stacking with larger separation to the hBN [31, 32, 20]. However, firm conclusions on the details of the superstructure are difficult to draw, because of the lack of knowledge of details of the van-der-Waals interaction [39].

The tip induced graphene QD can be moved across the graphene superstructure by moving the STM tip [41]. This allows to tune the QD properties, which we probe by tracking the position of the charging peaks within the superlattice. Therefore, we employ spatially resolved dI/dV spectra (I: tunneling current, V: tip voltage). The resulting maps of charging energies can be directly compared with the corresponding topographic maps recorded simultaneously (Fig. 2a). The charging peaks are fitted by Gaussians (Fig. 2b) for each QD center position $\underline{r}$, rendering maps of the local variation of the voltage $V_{\mathrm{P}n}(\underline{r})$ of the n^{th} peak, P_n (Fig. 2c, d). Typical variations between the center and the boundary of the hexagonal supercell are $\Delta V_{\mathrm{P}n} \approx 20\,\mathrm{mV}$. In order to relate this to an energy variation ΔE_n of a particular QD level, we employ a capacitive model yielding $\Delta E_n = \eta \cdot \Delta V_{\mathrm{P}n}$ with the lever arm $\eta \simeq 0.5$ [42]. The ΔE_n variations are primarily caused by the spatially varying adhesion energy across the supercell, which indeed varies on the 10 meV-scale according to extensive model calculations [31] (see below). Figure 2c and d additionally exhibit a long-range variation on the 50 nm scale (amplitude $\Delta V_{\mathrm{P}n} \simeq 40$ mV) which we attribute to the uncontrolled, long-range disorder potential of graphene on hBN with strength of about 20 meV and correlation length of about 50 nm. A similar disorder potential has been found previously [43, 44]. Note that we carefully avoid lifting of the graphene layer by the tip forces, i.e., we regularly record $I(z)$ curves (z: tip-sample distance) verifying that the current remains below the threshold where a slope change of $\ln(I(z))$ indicates lifting [45, 46].

Tracking orbital, valley and spin splitting

The group of the first four charging peaks, P1 to P4, is associated with the quadruplet belonging to the first hole orbital of the QD. During the charging of these levels, the QD exhibits a depth of about 100 meV and a width of about 50 nm as known from detailed Poisson calculations [42, 22]. The confined wave functions are labeled $\Psi_{\alpha,\tau,\sigma}$ with orbital quantum number $\alpha = 1$ for the first four peaks, valley quantum number $\tau = \pm\frac{1}{2}$ and spin quantum number $\sigma = \pm\frac{1}{2}$. Analogously, the next four peaks, P5 to P8, belong to the filling of the quadruplet $\Psi_{\alpha=2,\tau,\sigma}$. Subtracting the voltage of the highest peak of

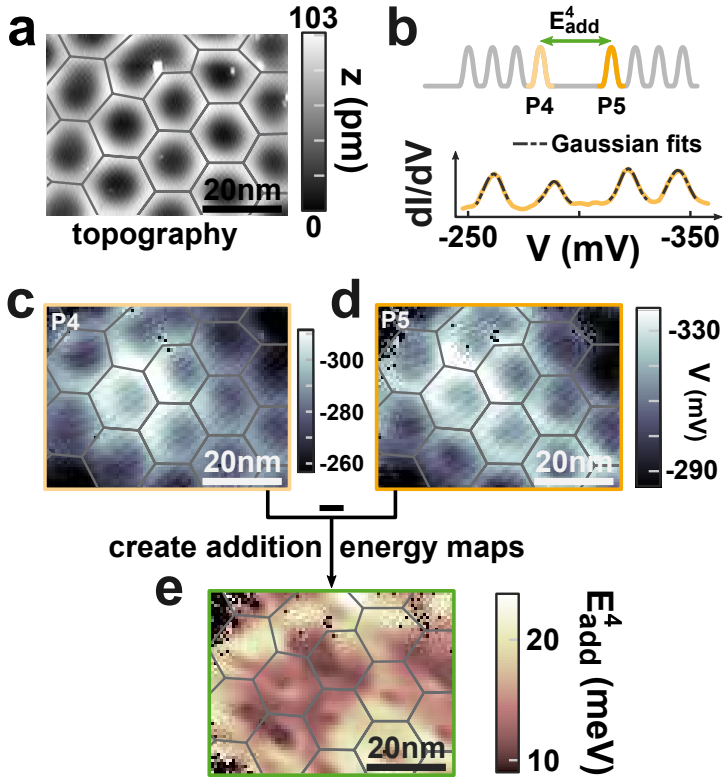

Figure 2: **Addition energy maps from dI/dV spectra**. **(a)** STM image of collinear graphene on h-BN, $V = 400\,\mathrm{mV}$, $I = 300\,\mathrm{pA}$, $B = 7\,\mathrm{T}$, $T = 8\,\mathrm{K}$. The overlay of grey lines marks the supercell boundary deduced from the topography. **(b)** Top: sketched charging peak sequence with highlighted peaks P4 and P5 separated by addition energy E^4_{add}. Bottom: typical dI/dV curve (yellow line) with Gaussian fits (dashed lines) used to determine peak voltages $V_{\mathrm{P}n}$. **(c,d)** Maps of V_{P4} (**c**) and V_{P5} (**d**) of the area of **a** with identical grey lines overlaid, same parameters for measurement of the map of dI/dV curves as in Fig. 1e. The slight shift of the observed patterns with respect to the grey lines is attributed to a small lateral shift (~ 2 nm) of the tunneling atom with respect to the center of the QD [40]. **(e)** E^4_{add} map deduced by $E^4_{\mathrm{add}}(\underline{r}) = \eta\,|V_{\mathrm{P5}}(\underline{r}) - V_{\mathrm{P4}}(\underline{r})|$, same grey lines as in **a**, **c**, **d**.

the first quadruplet V_{P4} from that of the lowest peak of the second, V_{P5}, and multiplying by η, yields the locally varying addition energy $E^4_{\mathrm{add}}(\underline{r}) = \eta|V_{\mathrm{P5}}(\underline{r}) - V_{\mathrm{P4}}(\underline{r})|$ (Fig. 2c–e). It consists of the charging energy $E^4_{\mathrm{C}}(\underline{r})$ and the energy difference $E_{2,-\frac{1}{2},-\frac{1}{2}}(\underline{r}) - E_{1,+\frac{1}{2},+\frac{1}{2}}(\underline{r})$. The latter includes the valley splitting $E_{\alpha,+\frac{1}{2},\sigma}(\underline{r}) - E_{\alpha,-\frac{1}{2},\sigma}(\underline{r})$ and the rather small Zeeman splitting $E_{\alpha,\tau,+\frac{1}{2}}(\underline{r}) - E_{\alpha,\tau,-\frac{1}{2}}(\underline{r}) = g\mu_{\mathrm{B}}B \approx 0.8\,\mathrm{meV}$ ($g = 2$: gyromagnetic factor of graphene, μ_{B}:

Bohr magneton), but is dominated by the orbital splitting $E_{2,\tau,\sigma}(\underline{r}) - E_{1,\tau,\sigma}(\underline{r})$ as known from tight binding calculations [22]. Since the wave function size does not change strongly as a function of $\underline{r}$ (supplementary movie), the spatial variation of $E_C^4(\underline{r})$ cannot explain the spatial variation of $E_{\mathrm{add}}^4(\underline{r})$ by about 100 %. Hence, $E_4^{\mathrm{add}}(\underline{r})$ (Fig. 2e) mostly maps out the orbital-energy spacing between $\alpha = 1$ and $\alpha = 2$, as the quantum dot is moved across the graphene superstructure. Periodic depressions in the center of the supercell reveal the influence of the superstructure on the orbital splitting, while the long-range structure in Fig. 2e (50 nm scale) is again attributed to the long-range potential disorder.

For clarity, we focus now on the second hole orbital shell $\alpha = 2$, while we provide more E_{add}^n maps in the supplementary sections 6 and 7. The local variation of the voltage peaks belonging to the $\alpha = 2$ quadruplet (V_{P5}, V_{P6} and V_{P7} in Fig. 3a) allows to map out valley and spin splittings. Surprisingly, the voltage maps, V_{P6} and V_{P7}, differ on length scales well below that of the supercell size (≈ 10 nm), and much smaller than the size of the QD wave function (diameter: ≈ 40 nm, calculated by our TB approach (Fig. 3a)). The addition energy maps (Fig. 3e−g) reveal details on the valley and spin splittings. Most remarkably, they display short-range supercell-periodic variations on the length scale of ≈ 3 nm. These variations appear as dark, ring-like structures around the AB stacking region of the supercell. The rings are similar in valley and spin addition energy maps, but slightly narrower in the latter E_{add}^5 and E_{add}^7 maps.

Analyzing the valley splitting maps

We analyze these remarkably strong nanometer scale variations by performing TB calculations [47, 34]. The calculations feature three major ingredients: the sublattice-independent local on-site potential $V_0(\underline{r})$ representing the spatially varying adhesion energy, the sublattice symmetry-breaking on-site potential $V_z(\underline{r})$ caused by the spatially varying stacking, and a locally varying hopping amplitude $\gamma(\underline{r})$ accounting for strain which also breaks sublattice symmetry [18, 46, 38]. We use an average distance between graphene and hBN of 3.3 Å, originating from DFT calculations employing the random phase approximation [30] and consistent with cross sectional electron microscopy data [48]. To obtain locally varying tight-binding parameters, we first employ a continuum model of graphene with known elastic constants [35] subject to the potential landscape from the hBN [31]. This reproduces the corrugation of 70 pm and the strain variation of 2 %, as visible in the STM data (Fig. 2a).[20] Based on the resulting membrane shape of the graphene layer, a molecular dynamics simulation using isotropic Lenard-Jones potentials is employed to obtain the atomically resolved strain, the variations in the local distance between hBN and graphene, and the local stacking configuration [42]. Using these input parameters, we determine $V_0(\underline{r})$, $V_z(\underline{r})$ and $\gamma(\underline{r})$ from our own DFT calculations [42]. The potentials and hopping parameters provide, in turn, the input to our third-nearest neighbor TB calculation of the QD states [47, 34, 22]. We emphasize that no freely adjustable

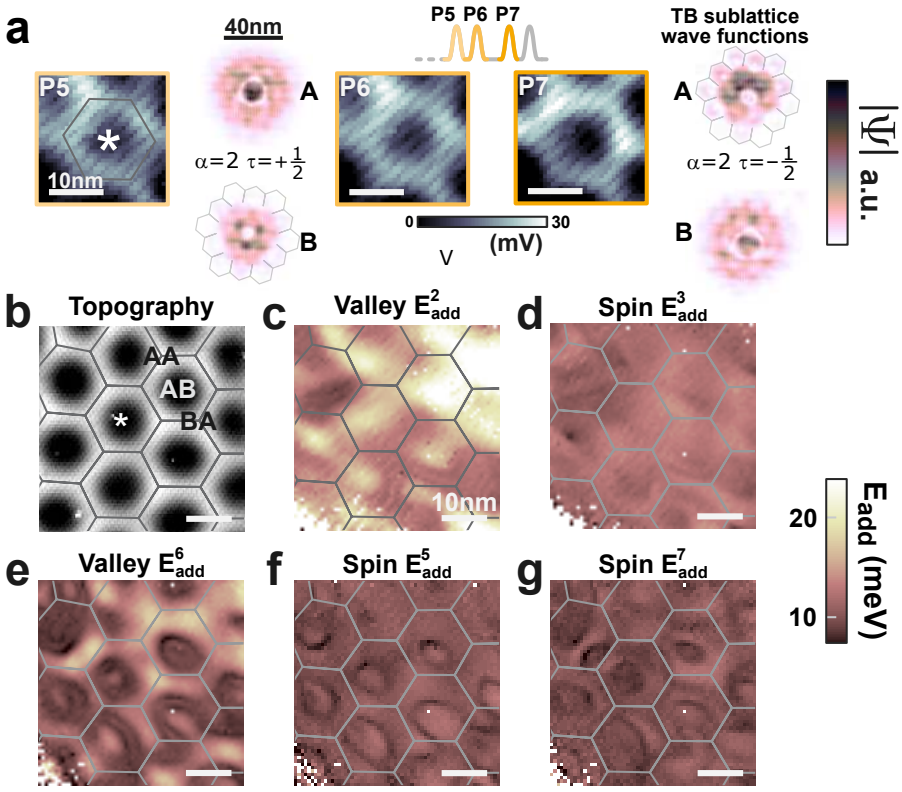

Figure 3: **Addition energy maps for spin and valley gaps**. **(a)** $V_{\mathrm{P}n}(\underline{r})$ displayed at identical contrast for $n = 5, 6, 7$. The corresponding charging sequence is sketched on top. The diagonal stripes are caused by the atomic lattice of graphene via a moiré effect as outlined in supplementary section 8. Asterisk in P5 marks the identical position in **b**. Also shown are the moduli of the wavefunctions for the second hole orbital, $\left|\Psi_{\alpha=2,\tau=+1/2}\right|$ and $\left|\Psi_{\alpha=2,\tau=-1/2}\right|$, decomposed into the two sublattice contributions, as marked by A and B, for the quantum dot with center in the AB stacking region. Grey honeycombs mark the unit cells of the graphene superstructure. Note the strongly different length scales of $|\Psi|$ maps and $V_{\mathrm{P}n}$ maps. **(b)** STM image of graphene on hBN including the area of **a**. Grey lines mark supercell boundaries. Different stacking areas (AA, AB, BA) are indicated, $V = 400\,\mathrm{mV}$, $I = 300\,\mathrm{pA}$. **(c)-(g)** $E^n_{\mathrm{add}}(\underline{r})$ maps exhibiting identical contrast and belonging to valley and spin gaps as marked, same grey lines as in **b**. Length of all unlabeled scale bars in (**a**−**g**): 10 nm. Same parameters for dI/dV spectra as in Fig. 1e.

parameter enters our simulation. More details are described in supplementary section 9-12.

In agreement with the experiment, the calculated energies of the two valley

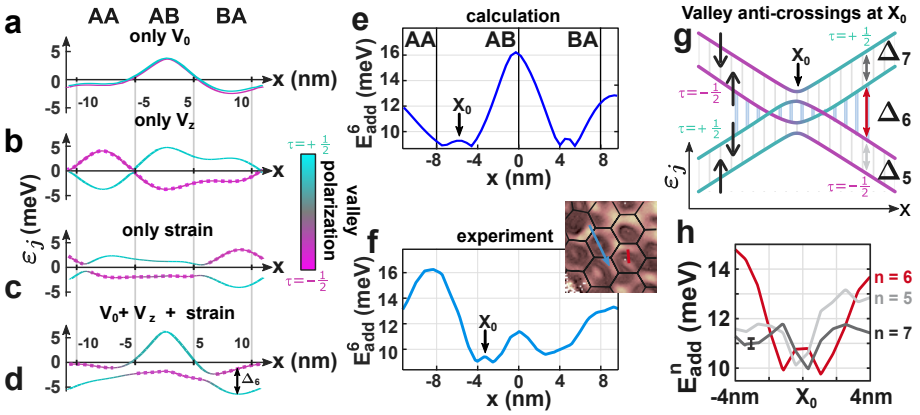

Figure 4: **Valley crossing**. **(a)**−**(d)** TB energies (ε_j) of the two valley states of the second QD hole orbital ($\alpha = 2$) as a function of the center position of the QD. Different stackings at this center along a high symmetry line of the superstructure are given on top. The valley polarization [42] is color coded. Panel (**a**) considers only the sublattice independent potential $V_0(\underline{r})$, (**b**) only the sublattice symmetry breaking on-site potential $V_z(\underline{r})$, (**c**) only the varying hopping parameter $\gamma(\underline{r})$ due to strain, and (**d**) the sum of all three contributions. The valley splitting Δ_6 determining the spatial variation in **e** is indicated by a double arrow in **d**, $B = 7$ T. **(e)** $E^6_{\rm add}$ as deduced from **d**, considering, in addition, a spatially constant charging energy and a spatially constant spin splitting [42]. **(f)** Experimental addition energy $E^6_{\rm add}$ along the arrow of the same color as in the inset (same $E^6_{\rm add}(\underline{r})$ map as Fig. 3d). The x-axis is aligned to the stackings marked in **e**. X_0 indicates a feature attributed to the influence of spin splitting at the valley crossing. The origin in **(a)**−**(f)** is chosen in the center of the AB region. **(g)** Schematic evolution of the state energies for a crossing of two valley states ($\tau = +1/2$: cyan, $\tau = -1/2$: magenta). A spatially constant spin splitting (levels marked by black spin arrows) is added. The resulting energy differences Δ_n are marked by double arrows. An artificial anticrossing is added at X_0. **(h)** Experimental $E^n_{\rm add}(\underline{r})$ along the red line in the inset of **f**, belonging to one preferential valley gap (red) and two spin gaps (grey). A typical error bar, resulting from the Gaussian fits of the dI/dV peaks, is shown.

states of the second orbital feature a pronounced variation with QD position (Fig. 4a−d). To disentangle the influence of strain and of the hBN substrate interaction, we analyze the contributions due to $V_0(\underline{r})$, $V_z(\underline{r})$, and $\gamma(\underline{r})$ separately. While V_0 (Fig. 4a) introduces local variations of the energy of the hole orbital $\alpha = 2$ along the path AA↔AB↔BA, it does not lift the fourfold valley and spin degeneracy. $V_z(\underline{r})$, by contrast, lifts the degeneracy between the two valley states $\Psi_{2,+\frac{1}{2},\sigma}$ and $\Psi_{2,-\frac{1}{2},\sigma}$ and even leads to an inversion of the energetic order in the AA region of the superlattice, i.e., a change of sign of

$E_{2,+\frac{1}{2},\sigma} - E_{2,-\frac{1}{2},\sigma}$ (Fig. 4b). However, only when the contribution of strain is accounted for through $\gamma(\underline{r})$, that inverts the sign of the valley splitting in the BA region (Fig. 4c), the correct level ordering with inversion in the AB region, as seen in our experiment, emerges (Fig. 4d).

Favorably, the addition energies in the TB model (Fig. 4e) and in the experiment (Fig. 4f) show the same variation of about 6 meV and the same order of maxima and minima along the displacement coordinate x. Hence, we attribute the periodically appearing rings encircling the AB region (Fig. 3e) as the positions of an inversion of valley ordering. Remaining quantitative differences between TB model and experiment (Fig. 4e, f) are attributed to disorder, most likely due to uncontrolled strains caused by the non-perfect collinear alignment between graphene and hBN. The resulting disorder is directly visible as irregularities in the unit cell of the superstructure (Fig. 2a, Fig. 3b) and also explains the irregular distortions of the rings around the AB region.

The assignment of the rings around the AB region to valley inversions is corroborated by the appearance of a small bump in the ring minimum, marked X_0 in Fig. 4e–h. It is found in theory and experiment with a height of less than 1 meV. The theoretical level diagram (Fig. 4g) provides a simple explanation: the bump is the result of the additional spin splitting during the passage through the crossing of valley levels. At X_0, E^6_{add} consists of E^6_{C} and the spin splitting $\left|E_{2,\tau,\frac{1}{2}} - E_{2,\tau,-\frac{1}{2}}\right| \approx 800\ \mu$eV reduced by anti-crossing contributions. In contrast, the two spatially offset crossings of valley states with different spins feature only E^6_{C}, resulting in the minima around the bump. Figure 4g also explains the rings in the spin splitting maps (Fig. 3f, g), which are simply the reduced Δ_5 and Δ_7 at X_0. The spatial alignment of the bump in Δ_6 and the minima in $\Delta_{5,7}$ are nicely corroborated by the experiment (Fig. 4h).

While we have focused here on the valley splitting of the second hole state, similar ring-like structures encircling the AB area are also found for the third hole orbital $\alpha = 3$ with tunability of the valley crossing up to 15 meV (Fig. S2) [42]. In contrast, the first hole orbital $\alpha = 1$ (Fig. 3c, e) exhibits a valley tunability of about 7 meV without inversion of the valley ordering. On the electron side, the additional charging of defects within the h-BN [49] complicates the analysis [50], but some ring-like structures indicating valley inversion can also be spotted [42]. Data recorded with another microtip at two different B fields exhibit very similar features (Fig. S3). Moreover, the energy range of valley tunability remains independent of B, corroborating that the valley tuning is caused by the substrate and not by the B field, which would increase, e.g., the exchange enhancement [42].

A simple estimate clarifies the resulting strength of the valley splitting of about 10 meV. The sublattice breaking interactions itself ($V_z(\underline{r})$, $\gamma(\underline{r})$) spatially vary by about 100 meV as known from DFT calculations [42]. Hence, shifting about 10% of the hole density of a state ($\propto |\Psi|^2$) from the unfavorable AB to the favorable AA region is sufficient to account for variations of the valley splitting of about 10 meV. Indeed, our detailed TB calculations find that the $\alpha = 2$ wave function covers about ten unit cells (Fig. 3a) and adjusts mainly

its distribution within the central unit cell to the changing potential landscape [see supplemental movie].

Conclusion

The revealed tunability of a valley splitting by up to 15 meV surpasses the highest reported values of valley tuning for a potentially nuclear spin free host material (Si/SiO_2, 500 µeV) [5] by more than an order of magnitude. Hence, it might be exploited at temperatures up to 4 K. Most intriguingly, the crossings of valley and spin levels as depicted in Fig. 4g can be used to initialize superposition states of spin and valley degrees of freedom [2, 51]. This could be the starting point to measure the coherence [52] of both types of states in graphene for the very first time. The required interaction of the levels rendering the depicted crossings into anti-crossings is naturally provided by the spatially varying sublattice potential coupling opposite valley states (Fig. 4d). We note in passing that the breaking of the valley degeneracy is also the central requirement for exchange-based spin qubits, which could provide an all electrical spin qubit operation in graphene [53]. A possible device setup for these purposes could employ side gates for moving gate-based QDs and, hence, for providing the valley tuning. Edge states, belonging to each LL, can provide tunable source and drain contacts (supplementary section 15).

Finally, we emphasize that the approach of designed van-der-Waals heterostructures [19, 20, 21] for a versatile tuning of electronic degrees of freedom might be extended to physical spin schemes by using an atomically varying spin orbit interaction as present, e.g., for graphene on WSe_2 [54].

Acknowledgements

The authors appreciate helpful discussions with C. Stampfer, H. Bluhm, R. Bindel, M. Liebmann, and K. Flöhr as well as the assisting during the measurements by A. Georgi. NMF, PN and MM acknowledge support from the European Union Seventh Framework Programme under Grant Agreement No. 696656 (Graphene Flagship) and the German Science foundation (Li 1050-2/2 through SPP-1459), LAC, JB and FL from the Austrian Fonds zur Förderung der wissenschaftlichen Forschung (FWF) through the SFB 041-ViCom and doctoral college Solids4Fun (W1243). TB calculations were performed on the Vienna Scientific Cluster. RVG, AKG and KSN also acknowledge support from EPSRC (Towards Engineering Grand Challenges and Fellowship programs), the Royal Society, US Army Research Office, US Navy Research Office, US Airforce Research Office. KSN is also grateful to ERC for support via Synergy grant Hetero2D. AKG was supported by Lloyds Register Foundation. PNI acknowledges the support from the Hungarian Academy of Sciences Lendület grant no. LP2017-9/2017.

Author contributions

NMF carried out the STM measurements with assistance of PNI and CH and evaluated the experimental data under supervision of PNI and MM; PNI has performed the strain calculations, while TR, FL, and LAC have contributed DFT and TB calculations; CRW, YC, RVG, AKG and KSN provided the sample; MM conceived and coordinated the project partly together with NMF, PNI and FL; the comparison between theory and experiment has been conducted by NMF, MM, FL, and PNI; MM, NMF, PNI and FL wrote the manuscript with contributions from all authors.

References

[1] T. D. Ladd, F. Jelezko, R. Laflamme, Y. Nakamura, C. Monroe, and J. L. O'Brien. Quantum computers. *Nature*, 464(7285):45–53, 2010.

[2] M. Pioro-Ladriere, T. Obata, Y. Tokura, Y. S. Shin, T. Kubo, K. Yoshida, T. Taniyama, and S. Tarucha. Electrically driven single-electron spin resonance in a slanting zeeman field. *Nat. Phys.*, 4(10):776–779, 2008.

[3] X. Wu, D. R. Ward, J. R. Prance, D. Kim, J. K. Gamble, R. T. Mohr, Z. Shi, D. E. Savage, M. G. Lagally, M. Friesen, S. N. Coppersmith, and M. A. Eriksson. Two-axis control of a singlet-triplet qubit with an integrated micromagnet. *Proc. Natl. Acad. Sci. U.S.A.*, 111(33):11938–11942, 2014.

[4] D. A. Abanin, S. V. Morozov, L. A. Ponomarenko, R. V. Gorbachev, A. S. Mayorov, M. I. Katsnelson, K. Watanabe, T. Taniguchi, K. S. Novoselov, L. S. Levitov, and A. K. Geim. Giant Nonlocality Near the Dirac Point in Graphene. *Science*, 332(6027):328–330, APR 15 2011.

[5] C. H. Yang, A. Rossi, R. Ruskov, N. S. Lai, F. A. Mohiyaddin, S. Lee, C. Tahan, G. Klimeck, A. Morello, and A. S. Dzurak. Spin-valley lifetimes in a silicon quantum dot with tunable valley splitting. *Nat. Commun.*, 4:2069, 2013.

[6] Y. Shimazaki, M. Yamamoto, I. V. Borzenets, K. Watanabe, T. Taniguchi, and S. Tarucha. Generation and detection of pure valley current by electrically induced Berry curvature in bilayer graphene. *Nat. Phys.*, 11(12):1032–1036, 2015.

[7] Mengqiao Sui, Guorui Chen, Liguo Ma, Wen-Yu Shan, Dai Tian, Kenji Watanabe, Takashi Taniguchi, Xiaofeng Jin, Wang Yao, Di Xiao, and Yuanbo Zhang. Gate-tunable topological valley transport in bilayer graphene. *Nat. Phys.*, 11(12):1027–1031, DEC 2015.

[8] Long Ju, Zhiwen Shi, Nityan Nair, Yinchuan Lv, Chenhao Jin, Jairo Velasco, Jr., Claudia Ojeda-Aristizabal, Hans A. Bechtel, Michael C. Martin, Alex Zettl, James Analytis, and Feng Wang. Topological valley transport at bilayer graphene domain walls. *Nature*, 520(7549):650–655, APR 30 2015.

[9] J. R. Wallbank, D. Ghazaryan, A. Misra, Y. Cao, J. S. Tu, B. A. Piot, M. Potemski, S. Pezzini, S. Wiedmann, U. Zeitler, T. L. M. Lane, S. V. Morozov, M. T. Greenaway, L. Eaves, A. K. Geim, V. I. Fal'ko, K. S. Novoselov, and A. Mishchenko. Tuning the valley and chiral quantum state of Dirac electrons in van der Waals heterostructures. *Science*, 353(6299):575–579, AUG 5 2016.

[10] R. Rahman, J. Verduijn, N. Kharche, G. P. Lansbergen, G. Klimeck, L. C. L. Hollenberg, and S. Rogge. Engineered valley-orbit splittings in

quantum-confined nanostructures in silicon. *Phys. Rev. B*, 83(19):195323, may 2011.

[11] T. Gokmen, Medini Padmanabhan, O. Gunawan, Y. P. Shkolnikov, K. Vakili, E. P. De Poortere, and M. Shayegan. Parallel magnetic-field tuning of valley splitting in alas two-dimensional electrons. *Phys. Rev. B*, 78:233306, Dec 2008.

[12] T. Kobayashi, J. van der Heijden, M. G. House, S. J. Hile, P. Asshoff, M. F. Gonzalez-Zalba, M. Vinet, M. Y. Simmons, and S. Rogge. Resonant tunneling spectroscopy of valley eigenstates on a donor-quantum dot coupled system. *Appl. Phys. Lett.*, 108(15):152102, APR 11 2016.

[13] John King Gamble, Patrick Harvey-Collard, N. Tobias Jacobson, Andrew D. Baczewski, Erik Nielsen, Leon Maurer, Inès Montaño, Martin Rudolph, M. S. Carroll, C. H. Yang, A. Rossi, A. S. Dzurak, and Richard P. Muller. Valley splitting of single-electron si MOS quantum dots. *Appl. Phys. Lett.*, 109(25):253101, dec 2016.

[14] P. Scarlino, E. Kawakami, T. Jullien, D. R. Ward, D. E. Savage, M. G. Lagally, Mark Friesen, S. N. Coppersmith, M. A. Eriksson, and L. M. K. Vandersypen. Dressed photon-orbital states in a quantum dot: Intervalley spin resonance. *Phys. Rev. B*, 95:165429, Apr 2017.

[15] X. Mi, Csaba G. Péterfalvi, Guido Burkard, and J. R. Petta. High-resolution valley spectroscopy of si quantum dots. *Phys. Rev. Lett.*, 119(17):176803, oct 2017.

[16] Di Xiao, Wang Yao, and Qian Niu. Valley-contrasting physics in graphene: Magnetic moment and topological transport. *Phys. Rev. Lett.*, 99(23):236809, DEC 7 2007.

[17] Dmytro Pesin and Allan H. MacDonald. Spintronics and pseudospintronics in graphene and topological insulators. *Nat. Mater.*, 11(5):409–416, MAY 2012.

[18] A. H. Castro Neto, F. Guinea, N. M. R. Peres, K. S. Novoselov, and A. K. Geim. The electronic properties of graphene. *Rev. Mod. Phys.*, 81(1):109–162, 2009.

[19] A. K. Geim and I. V. Grigorieva. Van der waals heterostructures. *Nature*, 499(7459):419–425, 2013.

[20] C. R. Woods, L. Britnell, A. Eckmann, R. S. Ma, J. C. Lu, H. M. Guo, X. Lin, G. L. Yu, Y. Cao, R. V. Gorbachev, A. V. Kretinin, J. Park, L. A. Ponomarenko, M. I. Katsnelson, Y. N. Gornostyrev, K. Watanabe, T. Taniguchi, C. Casiraghi, H. J. Gao, A. K. Geim, and K. S. Novoselov. Commensurate-incommensurate transition in graphene on hexagonal boron nitride. *Nat. Phys.*, 10(6):451–456, 2014.

[21] K. S. Novoselov, A. Mishchenko, A. Carvalho, and A. H. Castro Neto. 2D materials and van der Waals heterostructures. *Science*, 353(6298):461–470, JUL 29 2016.

[22] Nils M. Freitag, Larisa A. Chizhova, Peter Nemes-Incze, Colin R. Woods, Roman V. Gorbachev, Yang Cao, Andre K. Geim, Kostya S. Novoselov, Joachim Burgdörfer, Florian Libisch, and Markus Morgenstern. Electrostatically confined monolayer graphene quantum dots with orbital and valley splittings. *Nano Lett.*, 16(9):5798–5805, 2016.

[23] D. Bischoff, A. Varlet, P. Simonet, M. Eich, H. C. Overweg, T. Ihn, and K. Ensslin. Localized charge carriers in graphene nanodevices. *Appl. Phys. Rev.*, 2(3):031301, 2015.

[24] M. T. Allen, J. Martin, and A. Yacoby. Gate-defined quantum confinement in suspended bilayer graphene. *Nat. Commun.*, 3:934, 2012.

[25] A. M. Goossens, S. C. M. Driessen, T. A. Baart, K. Watanabe, T. Taniguchi, and L. M. K. Vandersypen. Gate-defined confinement in bilayer graphene-hexagonal boron nitride hybrid devices. *Nano Lett.*, 12(9):4656–4660, 2012.

[26] A. Müller, B. Kaestner, F. Hohls, T. Weimann, K. Pierz, and H. W. Schumacher. Bilayer graphene quantum dot defined by topgates. *J. Appl. Phys.*, 115(23):233710, 2014.

[27] A. S. Mayorov, R. V. Gorbachev, S. V. Morozov, L. Britnell, R. Jalil, L. A. Ponomarenko, P. Blake, K. S. Novoselov, K. Watanabe, T. Taniguchi, and A. K. Geim. Micrometer-scale ballistic transport in encapsulated graphene at room temperature. *Nano Lett.*, 11(6):2396–2399, 2011.

[28] A. V. Kretinin, Y. Cao, J. S. Tu, G. L. Yu, R. Jalil, K. S. Novoselov, S. J. Haigh, A. Gholinia, A. Mishchenko, M. Lozada, T. Georgiou, C. R. Woods, F. Withers, P. Blake, G. Eda, A. Wirsig, C. Hucho, K. Watanabe, T. Taniguchi, A. K. Geim, and R. V. Gorbachev. Electronic properties of graphene encapsulated with different two-dimensional atomic crystals. *Nano Lett.*, 14(6):3270–3276, 2014.

[29] Gianluca Giovannetti, Petr A. Khomyakov, Geert Brocks, Paul J. Kelly, and Jeroen van den Brink. Substrate-induced band gap in graphene on hexagonal boron nitride: Ab initio density functional calculations. *Phys. Rev. B*, 76:073103, Aug 2007.

[30] B Sachs, T O Wehling, M I Katsnelson, and A I Lichtenstein. Adhesion and electronic structure of graphene on hexagonal boron nitride substrates. *Phys. Rev. B*, 84:195414, 2011.

[31] M. M. van Wijk, A. Schuring, M. I. Katsnelson, and A. Fasolino. Moiré patterns as a probe of interplanar interactions for graphene on h-bn. *Phys. Rev. Lett.*, 113:135504, Sep 2014.

[32] Menno Bokdam, Taher Amlaki, Geert Brocks, and Paul J. Kelly. Band gaps in incommensurable graphene on hexagonal boron nitride. *Phys. Rev. B*, 89:201404, May 2014.

[33] Jeil Jung, Arnaud Raoux, Zhenhua Qiao, and A. H. MacDonald. Ab initio theory of moire superlattice bands in layered two-dimensional materials. *Phys. Rev. B*, 89:205414, May 2014.

[34] L. A. Chizhova, F. Libisch, and J. Burgdörfer. Graphene quantum dot on boron nitride: Dirac cone replica and hofstadter butterfly. *Phys. Rev. B*, 90(16):165404, 2014.

[35] P. San-Jose, A. Gutiérrez-Rubio, M. Sturla, and F. Guinea. Spontaneous strains and gap in graphene on boron nitride. *Phys. Rev. B*, 90(7):075428, 2014.

[36] G. J. Slotman, M. M. van Wijk, Pei-Liang Zhao, A. Fasolino, M. I. Katsnelson, and Shengjun Yuan. Effect of structural relaxation on the electronic structure of graphene on hexagonal boron nitride. *Phys. Rev. Lett.*, 115:186801, Oct 2015.

[37] Jin-Rong Xu, Ze-Yi Song, Chen-Guang Yuan, and Yu-Zhong Zhang. Interaction-induced metallic state in graphene on hexagonal boron nitride. *Phys. Rev. B*, 94:195103, Nov 2016.

[38] J. Jung, E. Laksono, A. M. DaSilva, A. H. MacDonald, M. Mucha-Kruczyski, and S. Adam. Moiré band model and band gaps of graphene on hexagonal boron nitride. *Phys. Rev. B*, 96:085442, June 2017.

[39] Alberto Ambrosetti, Nicola Ferri, Robert A. DiStasio, Jr., and Alexandre Tkatchenko. Wavelike charge density fluctuations and van der Waals interactions at the nanoscale. *Science*, 351(6278):1171–1176, MAR 11 2016.

[40] M. Morgenstern, D. Haude, V. Gudmundsson, Chr. Wittneven, R. Dombrowski, and R. Wiesendanger. Origin of landau oscillations observed in scanning tunneling spectroscopy on n-inas(110). *Phys. Rev. B*, 62:7257–7263, Sep 2000.

[41] R. Dombrowski, C. Steinebach, C. Wittneven, M. Morgenstern, and R. Wiesendanger. Tip-induced band bending by scanning tunneling spectroscopy of the states of the tip-induced quantum dot on inas(110). *Phys. Rev. B*, 59(12):8043–8048, 1999.

[42] N. Freitag, T. Reisch, L. A. Chizhova, P. Nemes-Incze, C. Holl, C. R. Woods, R. V. Gorbachev, Y. Cao, A. K. Geim, K. S. Novoselov, J. Burgdörfer, F. Libisch, and M. Morgenstern. *see supplementary information*, (1).

[43] J. M. Xue, J. Sanchez-Yamagishi, D. Bulmash, P. Jacquod, A. Deshpande, K. Watanabe, T. Taniguchi, P. Jarillo-Herrero, and B. J. LeRoy. Scanning tunnelling microscopy and spectroscopy of ultra-flat graphene on hexagonal boron nitride. *Nat. Mater.*, 10(4):282–285, 2011.

[44] R. Decker, Y. Wang, V. W. Brar, W. Regan, H. Z. Tsai, Q. Wu, W. Gannett, A. Zettl, and M. F. Crommie. Local electronic properties of graphene on a bn substrate via scanning tunneling microscopy. *Nano Lett.*, 11(6):2291–2295, 2011.

[45] T. Mashoff, M. Pratzer, V. Geringer, T. J. Echtermeyer, M. C. Lemme, M. Liebmann, and M. Morgenstern. Bistability and Oscillatory Motion of Natural Nanomembranes Appearing within Monolayer Graphene on Silicon Dioxide. *Nano Lett.*, 10(2):461–465, FEB 2010.

[46] Alexander Georgi, Peter Nemes-Incze, Ramon Carrillo-Bastos, Daiara Faria, Silvia Viola Kusminskiy, Dawei Zhai, Martin Schneider, Dinesh Subramaniam, Torge Mashoff, Nils M. Freitag, Marcus Liebmann, Marco Pratzer, Luger Wirtz, Colin R. Woods, Roman V. Gorbachey, Yang Cao, Kostya S. Novoselov, Nancy Sandier, and Markus Morgensternt. Tuning the Pseudospin Polarization of Graphene by a Pseudomagnetic Field. *Nano Lett.*, 17(4):2240–2245, APR 2017.

[47] F. Libisch, S. Rotter, J. Güttinger, C. Stampfer, and J. Burgdörfer. Transition to landau levels in graphene quantum dots. *Phys. Rev. B*, 81(24):245411, 2010.

[48] S. J. Haigh, A. Gholinia, R. Jalil, S. Romani, L. Britnell, D. C. Elias, K. S. Novoselov, L. A. Ponomarenko, A. K. Geim, and R. Gorbachev. Cross-sectional imaging of individual layers and buried interfaces of graphene-based heterostructures and superlattices. *Nat. Mater.*, 11(9):764–767, SEP 2012.

[49] D. Wong, J. Velasco, Jr., L. Ju, J. Lee, S. Kahn, H. Z. Tsai, C. Germany, T. Taniguchi, K. Watanabe, A. Zettl, F. Wang, and M. F. Crommie. Characterization and manipulation of individual defects in insulating hexagonal boron nitride using scanning tunnelling microscopy. *Nat. Nanotechnol.*, 10(11):949–953, 2015.

[50] Markus Morgenstern, Nils Freitag, Alexander Nent, Peter Nemes-Incze, and Marcus Liebmann. Graphene quantum dots probed by scanning tunneling microscopy. *Ann. d. Phys.*, 529(11):1700018, jul 2017.

[51] JR Petta, AC Johnson, JM Taylor, EA Laird, A Yacoby, MD Lukin, CM Marcus, MP Hanson, and AC Gossard. Coherent manipulation of coupled electron spins in semiconductor quantum dots. *Science*, 309(5744):2180–2184, SEP 30 2005.

[52] J. M. Elzerman, R. Hanson, L. H. Willems van Beveren, B. Witkamp, L. M. K. Vandersypen, and L. P. Kouwenhoven. Single-shot read-out of an individual electron spin in a quantum dot. *Nature*, 430(6998):431, jul 2004.

[53] B. Trauzettel, D. V. Bulaev, D. Loss, and G. Burkard. Spin qubits in graphene quantum dots. *Nat. Phys.*, 3(3):192–196, 2007.

[54] Zhe Wang, Dong-Keun Ki, Jun Yong Khoo, Diego Mauro, Helmuth Berger, Leonid S. Levitov, and Alberto F. Morpurgo. Origin and Magnitude of 'Designer' Spin-Orbit Interaction in Graphene on Semiconducting Transition Metal Dichalcogenides. *Phys. Rev. X*, 6(4):041020, OCT 26 2016.